Nature Communications

https://doi.org/10.1038/s41467-026-70720-9

Article in Press

Hygroscopicity-driven spontaneous sustainable direct lithium extraction

Received: 12 July 2025

Accepted: 2 March 2026

Cite this article as: Chen, H., Yang, M., Zheng, S. *et al.* Hygroscopicity-driven spontaneous sustainable direct lithium extraction. *Nat Commun* (2026). https://doi.org/10.1038/s41467-026-70720-9

Hongxu Chen, Meiqi Yang, Sunxiang Zheng, Ryan S. Kingsbury, Aashish S. Khandelwal, Hang Wang & Zhiyong Jason Ren

Hygroscopicity-driven spontaneous sustainable direct lithium extraction

Hongxu Chen[1,2], Meiqi Yang[1,2], Sunxiang Zheng[3], Ryan S. Kingsbury[1,2], Aashish S. Khandelwal[3], Hang Wang[3], Zhiyong Jason Ren[1,2,*]

[1]Department of Civil and Environmental Engineering, Princeton University, Princeton, NJ, 08544 USA

[2]Andlinger Center for Energy and the Environment, Princeton University, Princeton, NJ, 08544 USA

[3]Princeton Critical Minerals, Newark, NJ, 07102 USA

*Corresponding author: zjren@princeton.edu (Z. Ren).

Abstract

Current lithium extraction processes demand high inputs of energy, chemicals, and freshwater because they rely on non-spontaneous separation steps. To address these limitations, we introduce a spontaneous, hygroscopicity-driven direct lithium extraction method that leverages the unique entropy-increasing deliquescent behavior of lithium chloride hydrate (LHT) to extract and enrich lithium from solid deposits such as brine mining slags. At controlled relative humidities (12–30% RH), crystalline LHT selectively uptakes water moisture to form a lithium-enriched concentrate, while co-occurring salts (halite, sylvite, bischofite, gypsum) remain in the solid phase. This phase-selective deliquescence enables rapid solid-liquid separation without external water, reagents, or heating. By optimizing humidity and moisture flux, we achieve swift lithium recovery of up to 96% with concentrations reaching 97,000 ppm, far exceeding industrial grade requirements. We further validate the method's robustness across binary and multicomponent mixtures, as well as actual slag samples under mining conditions. The results demonstrate competitive performances over a wide range of feeding ratios and seasonal changes, and the extraction times only take minutes to hours as compared to months. This entropy-increasing, ambient-temperature modular process minimizes energy, chemical, and water use, and it offers broad resource tolerance for lithium extraction and mining waste valorization.

Introduction

Lithium (Li) is an essential element for batteries in electric vehicles, renewable energy storage, robots and many electronics[1-5]. The global Li demand is projected to triple by 2030, relative to the recent two years (2023-2025)[6,7], reaching above 2.5 million metric tons (Mt) of Li_2CO_3 equivalent (LCE)[7,8]; while current production remains below 0.6 Mt per year[9], creating a significant supply shortfall[10]. This gap cannot be offset by battery recycling alone but will be further exacerbated by the rising demand for large-scale energy storage, which is estimated to exceed 1.5 terawatt-hours by 2030 [11-13]. Current commercial Li production relies on solar evaporation of brine or mineral processing of hard rock ores. Brine evaporation is low-cost but slow (typically > 12 months) and water-intensive[14,15], while ore mining is faster but at the expense of high energy intensity, CO_2 emission, and tailing generation[16]. Emerging direct Li extraction (DLE) technologies promise high efficiency and low environmental impact[17,18], but to date they have struggled to scale from laboratory to field applications due to high capital and operational costs, as well as technical uncertainties[19,20].

The high cost and environmental impact associated with intensive energy, water, and chemical use by current technologies are largely due to the complexity of natural Li sources, which contain high concentrations of competing elements such as Na, K, Mg and Ca[15]. The essence of Li extraction is to harness the unique properties of Li against other elements to achieve separation. For example, the solvation energy[21], ionic size[22], charge density[23], and solubility[24] of Li have been widely explored to extract Li through ion exchange[25], ion sieving[26,27], and phase transformation mechanisms[28]. However, most of these methods are limited to Li separation from one specific kind of competing ions, such as tailored separation from either Na or Mg, which limits their applicability when multiple cations co-exist. The reason is rooted from the divergence in the trend of Li properties compared to different competing ions. For example, the hydration free energy of Li follows Mg > Ca > Li in divalent elements but Li > Na > K among the monovalent ions. Hence, adsorbents or membranes optimized for one pair often underperform against others[20].

Current mainstream Li extraction relies on either non-phase-transformation approaches such as electrochemical methods[29], adsorption[30], nanofiltration[26], solvent extraction[31], or aqueous-to-solid transformations such as evaporitic precipitation[32]. The fundamental principle of these techniques lies in redistributing the originally disordered ion mixtures to more ordered states so that Li can be selectively transported or retained for separation. Consequently, these processes are inherently non-spontaneous and entropy-reducing. Overcoming these thermodynamic barriers demands intensive inputs of water, energy, or chemicals and therefore leads to long processing times, high operational costs, and heavy reliance on specialized materials. When

producing one metric ton of Li_2CO_3, conventional mining consumes up to 60 m^3 of freshwater, 2.9 tons of chemicals and 1.8 MWh of electricity[33]. To surmount these limitations, technologies must both harness inherently spontaneous behaviors of Li and deliver robust separation performance across the diverse chemistries of real-world Li resources.

In this work, we introduce a sustainable, spontaneous method that has potential for extracting and enriching Li from a broad spectrum of solid resources, such as slag deposits from both brine- and ore-based mining as well as unconventional feedstocks such as spent battery electrodes and pharmaceutical wastes. In particular, industrial brine mining generates Li-bearing slags containing up to ~1 wt% Li (Fig. 1), yet these residues remain unexploited. We show that among the suite of constituent minerals that include LiCl hydrate (LHT), halite (NaCl), sylvite (KCl), bischofite ($MgCl_2·6H_2O$), and gypsum ($CaSO_4·2H_2O$), LHT stands out for its uniquely strong hygroscopicity. $CaCl_2$-based minerals are absent from the initial mineral mixtures because Ca occurs primarily as gypsum due to its low solubility and thermodynamic stability[34-36]. However, to assess the broader applicability of the hygroscopicity-driven separation mechanism, additional experiments involving $CaCl_2$ are performed and discussed in Supplementary Method 1, Supplementary Note 1 and Supplementary Fig. 1. By selectively leveraging rapid moisture uptake, our process enables LHT to deliquesce under mild conditions, allowing facile separation of Li from less hygroscopic phases and thereby driving an energy-efficient, water-minimal extraction route. Different from other processes, this presented method is entropy-increasing and can effectively reduce year-long passive leaching into a few-hour extraction, producing a Li-concentrated solution that can be collected via simple filtration, while less hygroscopic phases remain solid. Here, we use “entropy-increasing” to describe the deliquescence-driven LiCl extraction step and do not imply a net entropy increase over downstream Li upgrading from LiCl to Li_2CO_3 or LiOH, which would involve entropy-reducing crystallization and precipitation. Even from very low-grade feedstocks, this approach achieves over three orders of magnitude increase in Li purity. This process has low consumptions of freshwater, energy, and chemicals for Li extraction. It enables circular upgrading and valorization of industrial residues, mitigates the environmental impact of Li-bearing wastes to landfills and waterways, and provides a low-carbon complement to conventional extraction methods.

Results and Discussion

Humidity-controlled Li hygroscopic deliquescence recovery

To examine the hypothesis that Li can be effectively separated and recovered from mixed mineral deposits using hygroscopic deliquescence, we first quantify the stepwise moisture uptake in LHT and four commonly co-existing minerals, including bischofite, halite, sylvite and gypsum,

by exposing each solid mineral at controlled relative humidity (RH) from 12% to 96% in 6% increments (1 h per step). As shown in Fig. 2a, LHT exhibits measurable moisture uptake at RH as low as 12%, and the accumulative adsorption increases from 0.006 to 3.11 g H_2O g^{-1} LHT. In contrast, bischofite loses water at low RH (-0.0097 g H_2O g^{-1} bischofite at RH 12%) and only begins to adsorb moisture above RH ~30%, with the total adsorption amount around 1.09 g H_2O g^{-1} bischofite across the entire moisture spectrum. Halite, sylvite, and gypsum remain essentially inert until reaching their limiting RH values of ~78%, ~90%, and >96%, respectively. From these data, we identify each mineral's limiting RH and order them as LHT < bischofite << halite < sylvite < gypsum (Fig. 2b).

Because selective Li extraction requires LHT to dissolve while co-minerals remain solid, we designate RH 12-30% as the effective separation zone (Fig. 2b). To account for practical RH control variability, this zone is subdivided into three subzones: 12-18%, 18-24%, and 24-30%. In batch experiments of individual minerals, LHT yields progressively larger solution volumes in the higher RH subzone of 24-30% (Fig. 2c and 2d). All other minerals remain solid across these subzones. This demonstrates that ambient RH alone can drive selective dissolution of LHT, while preserving co-minerals in solids.

The essence of moisture uptake is aggregating free moisture from the ambient into clusters, which then dissolve LHT into collectable liquids. Built on this validated hypothesis, we evaluate the thermodynamics of moisture uptake in LHT by calculating the instantaneous free-energy change $\Delta G=\theta RT\ln a_w$, where θ is the equilibrium moisture uptake, a_w is the water activity (equal to the numerical value of RH), and $RT\ln a_w$ is the chemical potential of moisture equilibrated between the liquid and gaseous phases. More details can be found in Methods. Fig. 2e shows the LHT moisture uptake isotherm, and Fig. 2f illustrates ΔG against θ. Increasing RH from the lowest RH subzone (12-18%) through the intermediate (18-24%) to the highest subzone (24-30%) produces a ~16-fold increase in ΔG, indicating that higher RH substantially enhances the thermodynamic driving force for moisture uptake in LHT. Although ΔG plateaus overtime, these combined larger amounts of adsorption (Fig. 2e) and thermodynamic considerations identify RH 24-30% as the optimal control condition for selective Li extraction.

We discover that the moisture uptake behavior of LHT can be fitted to the D'Arcy-Watt model, which captures three terms that represent Langmuir adsorption ($KK'a_w/(1+Ka_w)$), linear adsorption (Ca_w) and multi-molecular adsorption ($kk'a_w/(1-ka_w)$) (Fig. 2f-g), respectively. Model parameters indicate that multi-molecular adsorption dominates at RH 12-18%, implying the surficial moisture clustering according to the D'Arcy-Watt's theory[37]. This stage represents the onset of mineral deliquescence, where surface hydration swiftly transitions into a dissolution phase[38-40]. Gradually Langmuir and linear adsorption increasingly contribute, signifying stronger

chemical binding and further hygroscopic growth towards complete mineral dissolution at higher RH subzones[41,42]. More details of modeling can be found in Methods and Supplementary Table 1 and 2.

Fast-flow hygroscopic uptake inhibits co-mineral dissolution

According to deliquescence theory, LHT in mixtures is expected to dissolve earlier than its pure form, because the inevitable eutonic effect would lower its critical humidity for deliquescence[40,41,43]. To probe the interactions of LHT's rapid moisture uptake with neighboring minerals, we create artificial contacts between LHT and each co-mineral, and image their interfaces in-situ by environmental SEM-EDS. As shown in Fig. 3a, pristine contacts exhibit sharp, water-free boundaries between LHT and halite, sylvite, bischofite or gypsum. After only 30 s at RH 24-30% (Fig. 3b), however, LHT aggregates moisture molecules to locally concentrate water, and the advancing liquid front visibly intrudes into adjacent minerals, suggesting that sustaining moisture uptake in LHT could gradually dissolve those co-minerals as a side effect. More time-series images during moisture uptake can be found in Supplementary Fig. 2-10.

To harvest the Li-rich solution as soon as it forms and mitigate its re-adsorption or mixing, we built a custom humidity-controlled chamber equipped with a dehumidifier, temperature controller, and vacuum-filtration configuration for timely solid-liquid separation (Fig. 3c). By drawing moisture through the mineral layer at controlled flow rates, we are able to regulate the moisture uptake kinetics. Fig. 3d illustrates the normalized uptake rate (R_{uptake}) against moisture flow rate (R_{flow}), revealing a clear Power-Law relationship. As R_{flow} increases from 4 to 20 m min^{-1}, R_{uptake} accelerates by ~9.4 times from 5.4×10^{-3} to 5.1×10^{-2} g H_2O g^{-1} min^{-1}, with a marked boost occurring above 10 m min^{-1}. A higher flow at 20 m min^{-1} not only facilitates moisture uptake but also strengthens vacuum-driven solid-liquid separation, cutting the time to collect the first batch of Li-rich solution from hours to mere minutes. At desired high R_{flow}, controlled packing density for salt loading would also impact R_{uptake} by reconciling its structural features. With equivalent LHT being tapped to half its bulk layer thickness (see Supplementary Method 2 for packing methods), the packing density rises from 0.41 to 0.84 g cm^{-3} by 2.05-fold (Supplementary Table 3). Under enhanced packing compressibility (Carr's Index climbs from 0-51.5), the theoretical porosity and flowability (Hausner ratio) are diminished by 25.8% and 106% correspondingly. Such structural densification attenuates moisture accumulation in LHT, with 58.2% reduction in R_{uptake} observed relative to the untapped loading (Supplementary Fig. 11). In this regard, the loose bulk without external tapping preserves structural merits that secure a more competitive kinetic profile for deliquescence.

Li extraction performance from binary mixtures

The performance of Li extraction from binary mineral mixtures is evaluated under optimal control conditions of RH 24-30% and moisture flow rate 20 m min^{-1}. For each mixture, LHT is first mixed with one co-mineral (halite, sylvite, bischofite or gypsum) at broad initial Li/M ("M" is Na, K, Mg or Ca) feeding ratios spanning from 1:100 to 50:1 in weight. Extraction proceeds via vacuum-driven batch-wise dripping for no more than four sequential batches (Fig. 4a-d). Lower initial Li/M feeding ratios typically exhaust in fewer batches. After each batch, the Li-rich solution is collected and the remaining solids advance to the next cycle, progressively depleting Li out of the solid phase (Supplementary Fig. 12).

We report four common performance metrics in Fig. 4a-d, including Li selectivity, solution Li/M ratio (purity), solution Li concentration, and accumulative recovery. The measurements and calculation details can be found in Methods. We can find for Li-predominant feeds (initial Li/M > 1:1), peak solution purities reach Li/Na ratio = 172.9, Li/K = 9128.1, Li/Mg = 347.5 and Li/Ca = 4742.3, respectively, demonstrating high Li purity in the collected solution. For M-predominant feeds (initial Li/M < 1:1), on the other hand, Li/M ratios in the collected solutions remain at high levels of ≥ 12-17 (Na), 3-12 (K), 0.1-0.7 (Mg) and 16.7-22.9 (Ca), respectively. Even for very low-grade feeds (initial Li/M ≤ 1:20), Li selectivity, defined by batch Li/M ratio in the collected solution relative to that in remaining solids from the previous batch, peaks at 2204.5 (Li/Na), 1436.1 (Li/K), 20.6 (Li/Mg) and 1621.3 (Li/Ca), illustrating strong performance against co-minerals (Fig. 4a-d). In Li/Na, Li/K and Li/Mg systems, the solution Li purities decline over successive batches, reflecting Li depletion in the solids. By contrast, Li/Ca mixtures display increasing solution Li/Ca ratios over the first three batches, which is a result of temporal gypsum viscous slurry formation upon contacting water in LHT (Supplementary Fig. 13-16). When more moisture is adsorbed by LHT, the slurry becomes fluidic, which in turn promotes Li solution drainage. In addition, we notice a lower Li/Mg selectivity relative to other mixtures, reflecting bischofite is more sensitive to the hygroscopic growth of LHT. We therefore hypothesize that applying stronger vacuum filtration for faster solid-liquid separation, or testing on more hydrophilic filters for accelerated liquid adsorption could further suppress competing effects especially for low-grade feeds and unleash extraction performances.

Li concentrations in collected solutions span 72.4-97.8 g L^{-1} (Li/Na), 72.6-95.2 g L^{-1} (Li/K), 11.6-88.7 g L^{-1} (Li/Mg) and 56.1-95.5 g L^{-1} (Li/Ca) across different initial feeding ratios. For the highest-grade Li/M feed (50:1), 95.1-96.9% of Li is recovered within 0.8-1.2 h, and even for low-grade feeds, the process still achieves 81.3-90.3% (Li/Na), 80.9-92.7% (Li/K), 46.0-80.6% (Li/Mg) and 64.6-73.3% (Li/Ca) recovery within 3.1 h. Importantly, most Li is harvested at peak purities.

For example, in Li/Na systems, 53.1-93.5% of Li is recovered within just 0.1-0.6 h, and the collected solutions exhibit Li/Na ratio of 114.2-172.9 (Fig. 4a). Likewise, in Li/K systems, 81.6-92.9% of Li is recovered in 0.3-0.5 h at Li/K purities of 330.2-7934.0; in Li/Mg systems, 86.1-96.2% is recovered in 0.1-0.6 h at Li/Mg = 29.3-347.5; and in Li/Ca systems, 54.1-69.6% is recovered in 0.4-0.9 h at Li/Ca = 428.3-4742.3 (Fig. 4b-d).

Because strong hygroscopicity is an intrinsic property of mineral LHT, our humidity-controlled extraction principle, and the associated configuration design, can be directly extended to more complex, multi-component Li resources.

Li extraction from mining slags in environmental conditions

Industrial Li mining operations produce large volumes of Li-bearing solid slags that are challenging to recycle because of diverse components and chemistries. For example, brine-based extraction generates slags typically contain ~1 wt% Li among all species and impurities, which are currently left unexploited. To demonstrate industrial applicability, we process a multi-component Li-bearing slag from a brine operation, which contains 6.4 wt% Li, 8.3 wt% Na, 2.6 wt% K, 82.6 wt% Mg, and 0.1 wt% Ca relatively across these five elements (mixed as LHT, halite, sylvite, bischofite, gypsum, and complex mutual phases such as bischofite-sylvite dual-salts; Supplementary Fig. 17), along with minor components such as boron and insoluble matters. Under control condition (RH 24-30%, moisture flow 20 m min^{-1}), three successive vacuum-driven batches recover 83.5 % of total Li in just 1 h (Fig. 5a). Notably, Batch 1 alone recovers 71.2% of Li in only 0.08 h, where Li purity is 91.9, 117.6, 0.34 and 261.3 times that of Na, K, Mg and Ca in the collected solution. Subsequent Batch 2 and 3 further enrich Li/Na to 137.6, Li/K to 127.5, Li/Mg to 13.1, and Li/Ca to 12.8, with solution Li concentrations of 24.7, 23.1 and 19.3 g L^{-1}. These numbers are several times higher than typical preconcentrated Li concentrates for industrial Li_2CO_3 production[15,44].

Most Li brine operations are located in hyper-arid basins around the world, for example, Salar de Atacama in Chile, Silver Peak in the U.S., and Zabuye Salt Lake in China (Supplementary Fig. 18). Because Li hygroscopicity drives extraction at low RHs, we exploit the operational performances under natural conditions in Atacama, where the averaged seasonal RH (13.3-23.8%) and temperature (11.7-20.9°C) both fall below our lab control, although higher perturbations are observed in nature (Fig. 5b and Methods). Beyond complex components, these environmental settings also represent unfavorable yet realistic operating conditions, in which low temperature and fluctuating humidity impose a more rigorous assessment on the general applicability of this hygroscopicity-driven approach. It is found that the total Li recovery across the four seasons remain as high as 84.5%, 84.0%, 90.2% and 87.7%, with processing time below 3.0,

1.2, 1.3 and 1.6 h, respectively. Moreover, even a single Batch 1 is able to recover 65.3%, 57.3%, 67.1% and 53.8% of Li, in around 0.9, 0.3, 0.4, and 0.6 h (Fig. 5c-f). These results confirm that our humidity-controlled extraction performs robustly under real-world, low-humidity field conditions.

Under spring, fall and winter profiles (Fig. 5c-f), the cooler temperatures lead to reduced sylvite solubility and as a result elevate Li/K separation performance: Li/K ratios in solution climb to 220.5, 265.6 and 704.1 (up to 87.5%, 126.0% and 498.7% vs. control), translating into higher Li/K selectivity of 289.3, 342.3 and 449.5. Solution Li/Mg ratios show similar trends, rising by 164.0% (spring) and 147.0% (winter) related to the control. In terms of humidity, a low moisture content may restrain the amount of moisture uptake but can lead to higher Li concentrations in collected solutions, which is favorable for Li enrichment though only slightly extends the processing time. For example, under spring condition (Fig. 5c), recovered Li concentration ranges in 25.8-35.2 g L^{-1}, which is ~40% higher than the control group (Fig. 5a). Overall, these results indicate this hygroscopicity approach can be harnessed under natural low-humidity conditions to achieve rapid, high-purity Li extraction from complex industrial mixed resources.

Modular scale-up demonstration

We further evaluate the scale-up potential of the hygroscopicity-driven extraction using a vertical shell-side filtration design (Fig. 6a). Industrial Li-bearing slags are packed into the hollow interlayer of an inward double-frame reactor. Application of vacuum to the inner chamber draws moisture-laden air through the slag bed, where hygroscopic uptake induces deliquescence and generates Li concentrates that drain spontaneously into the bottom collector under gravity (Fig. 6b). Detailed information on modular configuration and dimensions is provided in Supplementary Fig. 19 and Supplementary Table 4. This modular setup exhibits rapid processing especially under favorable conditions (RH 24-30%). Increasing the cross-slag air flow from 50 to 100 L min^{-1} raises the slag processing rate from 3.65 to 8.01 kg m^{-1} d^{-1} when normalized by module height (Fig. 6c, see Methods for calculation details), yielding up to 0.28 L d^{-1} of Li concentrates. Across this range of air flows, the module achieves high area-normalized Li extraction rates (0.08-0.25 kg m^{-2} d^{-1}) and elevated Li concentrations in collected solutions (14,220-22,730 ppm), outperforming reported Li extraction technologies by 1-3 orders of magnitude (Fig. 6d). Notably, the yield LiCl obtained in the scale-up module remains > 2 times more concentrated than those of typical preconcentrated LiCl solutions qualified for further industrial Li_2CO_3 upgrading[15,44].

The hygroscopicity-driven extraction establishes a rapid, low-carbon and resource-efficient route of high-purity Li recovery with minimal energy, water, or chemical uses. Distinct from current

chemical and energy intensive processes that use specially synthesized materials, harsh reagents and large amounts of freshwater, this method exploits the intrinsic spontaneous deliquescence of Li to selectively dissolve LHT in a few hours without external reagents or heat throughout operation. Its simple and modular setup can be retrofitted to existing workflows or paired with humidity-controlled adsorption or nanofiltration to further improve purity. This hygroscopicity-driven strategy can also extend beyond slags to sulfate-type salt lakes, seawater, and various Li-bearing solids. Notably, Li_2SO_4 exhibits a limiting RH (~60%) in mixtures that can be well separated from $MgSO_4$ (> 80%)[45,46], providing an even larger RH window than chloride systems and highlighting sulfate resources' particular favorability for this approach. Looking forward, we envision this approach to be beneficial for both controlled factory setup and direct deployment under natural climate conditions. To address foreseeable challenges relative to large-scale efficiency or environmental perturbations, research on humidity tuning, flow dynamics, pretreatment, multi-component mutual interactions, modular encapsulation, and reactor development is needed and more feedstocks such as hard rock ores, spent battery electrodes, and tailings can be tested under controlled environments or onsite field conditions. For a clear prospect, we also provide a shortlist on potential process controls that could be further investigated (see Supplementary Table 5). Together, the findings in this first study point to a versatile and sustainable paradigm for mineral recovery and derisked Li supply in the most water-stressed mining regions worldwide.

Methods

Materials and reagents

All salts employed in current setup as laboratory systems are analytical grade with conservative control margins to ensure reproducibility, including LHT in ≥ 99.99%, NaCl in ≥ 99%, KCl in 99-100.5%, $MgCl_2·6H_2O$ in 99-102%, $CaSO_4·2H_2O$ in ≥ 99%, and $CaCl_4·2H_2O$ in ≥ 99%, as stated by the suppliers. Multi-component Li-bearing slag mixtures used for industrial and scale-up modular demonstration are sourced from a brine operation with compositions and concentrations disclosed above in the main text.

Isothermal moisture uptake measurements

Isothermal moisture uptake in minerals is quantified using an analytical Dynamic Vapor Sorption (DVS, DSA-0184@MFG, TA Instrument) system with an accuracy of 10 ppm in mass change. Before measurement, ~25 mg of LHT, halite, sylvite, bischofite and gypsum are loaded onto separate sample pans within the DVS system, with the background environmental condition set to temperature 25°C and RH 6% for initialization. For each measurement, we take an enforced

pre-drying procedure to eliminate the influence of system background condition on mineral moisture uptake. Each mineral is dried at 60°C until the mass fluctuation is stabilized within ± 1% for at least 1 h.

To determine each mineral's limiting RH (Fig. 2a), we perform a stepped RH sweeping from 12% up to 96% in 6% increments. At each RH step, the sample is held for 1 h and the mass change (Δm) is recorded as the corresponding amount of water adsorbed during that interval. To identify the equilibrium moisture uptake in LHT across three RH subzones (Fig. 2e), we measure the full adsorption isotherm of LHT over the effective extraction window (RH 12-30%; Fig. 2e) by incrementing RH 1%. At each step, the sample is held until mass change stabilized within ± 1% for at least 1 h, ensuring true equilibrium uptake.

Thermodynamic analysis and mechanistic modeling

The thermodynamics of LHT moisture uptake involves the investigation of adsorption free energy and adsorption mechanisms, both of which are derived from the isothermal adsorption equilibrium. According to thermodynamic equilibrium, the instantaneous free energy change (ΔG) of moisture uptake at each RH step should be represented by the product of moisture chemical potential and the amount of equilibrium moisture uptake:

$$\Delta G_{\text{moisture uptake}} = \theta RT \ln a_{\text{w}} \tag{1}$$

where the amount of moisture uptake per unit LHT (θ) is determined from isothermal adsorption equilibrium, and water activity (a_{w}) refers to the equilibrium ratio between the partial vapor pressure of atmospheric moisture and the saturation vapor pressure of liquid water adsorbed in the mineral, which is equal to the numerical value of RH. A D'Arcy-Watt model is established to investigate the binding mechanisms between LHT and moisture molecules[51,52]:

$$\theta = \frac{KK' a_{\text{w}}}{1 + K a_{\text{w}}} + C a_{\text{w}} + \frac{k k' a_{\text{w}}}{1 - k a_{\text{w}}} \tag{2}$$

This model is employed as a mechanistic framework across the full humidity range to capture the net outcome of ionic dissociation, salt dissolution and solution formation through hygroscopic moisture uptake. Based on thermodynamic principles, the θ in LHT is made up of three terms in sequence: 1) Langmuir adsorption that implies strong chemical bindings where K and K' represent the binding affinity and the number of strong binding sites; 2) linear adsorption that implies weak bindings and mineral dissolution where C is a combined measure of the binding affinity and the number of weak binding sites; and 3) multi-molecular adsorption that implies bulk free moisture clustering where k and k' represent the binding affinity and the number of multi-molecular binding sites. Because deliquescence manifests as a continuous solution growth profile rather than a sharp phase transition, by fitting the model with equilibrium isothermal adsorption, the potential dominant

contribution of these three adsorption can be attained. Nonlinear regression (Supplementary Tables 1 and 2) yields excellent fittings (R^2 > 0.996), allowing us to quantify each term's contribution across RH subzones.

Kinetic analysis and moisture flow rate

The simplified binary mineral contact (Fig. 3a and b) is designed to illustrate the necessity of rapid solid-liquid separation in mitigating the mixing between LHT hygroscopic growth and co-minerals. The contacts are prepared by gentle mechanical mixing of finely ground mineral powders (typically <75 μm) to ensure close solid-solid interfaces without excessive tapping, structural modification, or partial dissolution. Co-precipitation or solution equilibration is excluded as the objective is to emulate the physical adjacency and interfacial behavior of representative mineral phases rather than chemical homogenization.

The purpose of moisture uptake kinetics is to examine the moisture flow rate that can accelerate the uptake in minerals and facilitate solid-liquid separation for Li extraction. The LHT is placed atop the vacuum filter, and the moisture flow rate across the LHT is regulated by the outlet rate of vacuum system. A flowmeter with an accuracy to ± 0.01 L min^{-1} ensures precise control of the outlet rate. The moisture uptake rate is measured at the optimal RH subzone 24-30% and the moisture flow rate across LHT is varied from 4 to 20 m min^{-1} (i.e. 4, 5, 6, 8, 10, 12, 14, 16, 18 and 20 m min^{-1}). A flow rate below 4 m min^{-1} fails to achieve sufficient solid-liquid separation due to inadequate negative pressure. At each flow rate, the mass change of LHT, representing the amount of moisture uptake, is recorded every 5 min until the first droplet of Li solution obtained. A pseudo-first-order kinetic adsorption model based on mass change over time is developed to derive the moisture uptake rate. The moisture uptake rate is normalized by the amount of LHT involved. The attained trend is well identified to showcase the Power-Law behavior, which follows the exponential relationship as:

$$R_{\text{uptake}} = A\exp(NR_{\text{flow}}) \quad (3)$$

where R_{uptake} and R_{flow} denote the normalized moisture uptake rate, and the moisture feeding flow rate, respectively. A is the proportionality coefficient and N is the Power-Law exponent that describes the sensitivity of adsorption to feeding rate.

The in-situ imaging of the micro-boundaries between LHT and other minerals is enabled by an environmental SEM (ESEM, Quanta 200 FEG). The ESEM features a Peltier stage, allowing the imaging of real-time morphology of minerals when interacting with moisture. The internal temperature and RH are fixed at 25°C and 27% (the medium value between 24% and 30%). Due to the low-conductive nature of minerals, a low vacuum mode is adopted with an internal pressure maintained between 0.1-1.0 torr.

Li extraction and recovery

Li extraction and recovery is first carried out in binary mineral mixtures with varied initial feeding ratios under control conditions (RH 24-30% and flow rate 20 m min^{-1}). The potential of applications in arid regions are then demonstrated using a real-world industrial slag with complex multi-components. The setup for Li extraction is displayed in Fig. 3c, and Li is recovered in the form of Li-rich solution in sequential batches (Fig. 1).

For binary mineral mixtures, LHT is individually mixed with halite, sylvite, bischofite or gypsum at the initial Li:M feeding ratio of 50:1 to 10:1, 5:1, 1:1, 1:5, 1:10, 1:20, 1:50 and 1:100 in weight (M = Na, K, Mg or Ca). At the end of each batch (*n*), the Li/M ratio in the collected liquid solution ($\mathrm{LR}^{\mathrm{n}}_{\mathrm{Li/M}}$), the Li/M ratio of the solids remaining atop the filter ($\mathrm{SR}^{\mathrm{n}}_{\mathrm{Li/M}}$), and the Li concentration in the collected solution ($c^{\mathrm{n}}_{\mathrm{Li}}$) are measured. Li selectivity at Batch *n* is defined as:

$$\text{Li selectivity} = \frac{\mathrm{LR}^{\mathrm{n}}_{\mathrm{Li/M}}}{\mathrm{SR}^{\mathrm{n-1}}_{\mathrm{Li/M}}} \tag{4}$$

Li recovery of batch *n* is calculated by:

$$\text{Li recovery} = \frac{\text{Li in the collected solution}}{\text{Total Li in initial solid mixture}} \times 100\% \tag{5}$$

The accumulative Li recovery corresponds to the summation of Li recovery up to the current batch.

For the industrial slag demonstration, XRD analysis (Supplementary Fig. 17) is used to characterize the major compositions of the sample, a mixture of LHT, halite, sylvite, bischofite and gypsum. Extractions are performed first under control conditions (25°C, RH 24-30%, flow 20 m min^{-1}), and then under simulated climates of a brine mining site in Salar de Atacama. Based on two-year meteorological records at the evaporation ponds, seasonal parameters are set as follows. Spring (Dec. –Feb.): RH 13.3 ± 4.5 %, temperature 16.7 ± 2.9 °C, wind 2.3 ± 1.2 m s^{-1}. Summer (Mar. –May): RH 23.2 % ± 9.3 %, temperature 20.9 ± 1.7 °C, wind 3.3 ± 1.3 m s^{-1}. Fall (Jun.–Aug.): RH 23.8 % ± 9.6 %, temperature 17.6 ± 3.0 °C, wind 2.1 ± 1.2 m s^{-1}. Winter (Sep.–Nov.): RH 15.3 % ± 4.5 %, temperature 11.7 ± 2.1 °C, wind 1.4 ± 0.9 m s^{-1}. Two commercial fans provide advection over the mineral bed and within the chamber. Wind speed is adjusted via fan orientation and position and calibrated with an anemometer (± 0.01 m s^{-1}).

For the scale-up modular demonstration, the slag processing rate is defined as the mass of fully packed slag normalized by the module height and the duration of a single operation:

$$\text{Slag processing rate} = \frac{\text{Loading mass}}{\text{Module height} \times \text{Operation time}} \tag{6}$$

The Li concentrate yield is calculated as the total volume of Li concentrate produced per unit operation duration:

$$\text{Li concentrate yield} = \frac{\text{Total volume of produced Li concentrates}}{\text{Operation time}} \quad (7)$$

The Li extraction rate is calculated as the mass of recovered Li normalized by the filtration area (i.e. side area of the inner frame) in the module, and the operation duration.

$$\text{Li extraction rate} = \frac{\text{Mass of recovered Li}}{\text{Module filtration are} \times \text{Operation time}} \quad (8)$$

Data Availability

All data are presented in the article or the supplementary information. Source data are provided with this paper.

Code Availability

Python was used to create Supplementary Fig. 18, and the codes are available upon reasonable request.

References

1 Humanity needs to diversify its lithium sources. *Nature* **637**, 1021-1022, doi:10.1038/d41586-025-00213-0 (2025).

2 Chen, S. *et al.* External Li supply reshapes Li deficiency and lifetime limit of batteries. *Nature* **638**, 676-683, doi:10.1038/s41586-024-08465-y (2025).

3 Castelvecchi, D. Electric cars and batteries: how will the world produce enough? *Nature* **596**, 336-339, doi:10.1038/d41586-021-02222-1 (2021).

4 Guelfo, J. L. *et al.* Lithium-ion battery components are at the nexus of sustainable energy and environmental release of per- and polyfluoroalkyl substances. *Nature Communications* **15**, 5548, doi:10.1038/s41467-024-49753-5 (2024).

5 Greim, P., Solomon, A. A. & Breyer, C. Assessment of lithium criticality in the global energy transition and addressing policy gaps in transportation. *Nature Communications* **11**, 4570, doi:10.1038/s41467-020-18402-y (2020).

6 IEA. Global lithium demand in the Net Zero Scenario, 2030-2040. *IEA, Paris*, https://www.iea.org/data-and-statistics/charts/global-lithium-demand-in-the-net-zero-scenario-2023-2040 (2024).

7 Unlocking lithium's potential: How to do it sustainably in Europe. *Transport and Environment*, https://www.transportenvironment.org/articles/unlocking-lithiums-potential-how-to-do-it-sustainably-in-europe#:~:text=As%20a%20critical%20element%20in,lithium%20carbonate%20equivalent)%20by%202030. (2024).

8 Lithium mining: How new production technologies could fuel the global EV revolution. *McKinsey & Company*, https://www.mckinsey.com/industries/metals-and-mining/our-insights/lithium-mining-how-new-production-technologies-could-fuel-the-global-ev-revolution (2022).

9 IEA. Global Critical Minerals Outlook 2024. *IEA, Paris*, https://www.iea.org/reports/global-critical-minerals-outlook-2024 (2024).

10 Raw materials for a truly green future. *Nature Reviews Materials* **6**, 455-455, doi:10.1038/s41578-021-00333-9 (2021).

11 IEA. Batteries and Secure Energy Transitions. *IEA, Paris*, https://www.iea.org/reports/batteries-and-secure-energy-transitions (2024).

12 UN. Global Energy Storage and Grids Pledge. *COP29, Baku*, https://cop29.az/en/pages/cop29-global-energy-storage-and-grids-pledge (2024).

13 Frith, J. T., Lacey, M. J. & Ulissi, U. A non-academic perspective on the future of lithium-based batteries. *Nature Communications* **14**, 420, doi:10.1038/s41467-023-35933-2 (2023).

14 Darling, S. B. The brine of the times. *Science* **385**, 1421-1422, doi:10.1126/science.ads3699 (2024).

15 Vera, M. L., Torres, W. R., Galli, C. I., Chagnes, A. & Flexer, V. Environmental impact of direct lithium extraction from brines. *Nature Reviews Earth & Environment* **4**, 149-165, doi:10.1038/s43017-022-00387-5 (2023).

16 Haddad, A. Z. *et al.* How to make lithium extraction cleaner, faster and cheaper - in six steps. *Nature* **616**, 245-248, doi:10.1038/d41586-023-00978-2 (2023).

17 Zeng, Y. *et al.* Electrochemically Mediated Lithium Extraction for Energy and Environmental Sustainability. *Advanced Functional Materials* **34**, 2400416, doi:10.1002/adfm.202400416 (2024).

18 Pell, R. *et al.* Towards sustainable extraction of technology materials through integrated approaches. *Nature Reviews Earth & Environment* **2**, 665-679, doi:10.1038/s43017-021-00211-6 (2021).

19 Schenker, V., Bayer, P., Oberschelp, C. & Pfister, S. Is lithium from geothermal brines the sustainable solution for Li-ion batteries? *Renewable and Sustainable Energy Reviews* **199**, 114456, doi:10.1016/j.rser.2024.114456 (2024).

20 Yang, S., Wang, Y., Pan, H., He, P. & Zhou, H. Lithium extraction from low-quality brines. *Nature* **636**, 309-321, doi:10.1038/s41586-024-08117-1 (2024).

21 Wu, X. *et al.* Sustainable lithium extraction enabled by responsive metal-organic frameworks with ion-sieving adsorption effects. *Proceedings of the National Academy of Sciences* **121**, e2309852121, doi:10.1073/pnas.2309852121 (2024).

22 Peng, Q. *et al.* Extreme Li-Mg selectivity via precise ion size differentiation of polyamide membrane. *Nature Communications* **15**, 2505, doi:10.1038/s41467-024-46887-4 (2024).

23 Li, B. *et al.* Elevating the Li–Mg Separation Performance of LATP Solid Superionic with Enhanced Local Positive Charge Density. *Advanced Functional Materials* **n/a**, 2425353, doi:10.1002/adfm.202425353 (2025).

24 Chen, X. *et al.* Spatially separated crystallization for selective lithium extraction from saline water. *Nature Water* **1**, 808-817, doi:10.1038/s44221-023-00131-3 (2023).

25 Kong, L. *et al.* Electro-driven direct lithium extraction from geothermal brines to generate battery-grade lithium hydroxide. *Nature Communications* **16**, 806, doi:10.1038/s41467-025-56071-x (2025).

26 Zhang, S. *et al.* Solar-driven membrane separation for direct lithium extraction from artificial salt-lake brine. *Nature Communications* **15**, 238, doi:10.1038/s41467-023-44625-w (2024).

27 Yang, D. *et al.* Solution-processable polymer membranes with hydrophilic subnanometre pores for sustainable lithium extraction. *Nature Water* **3**, 319-333, doi:10.1038/s44221-025-00398-8 (2025).

28 Song, Y. *et al.* Solar transpiration–powered lithium extraction and storage. *Science* **385**, 1444-1449, doi:10.1126/science.adm7034 (2024).

29 Xiong, Y. *et al.* Electrochemical lithium extraction from aqueous sources. *Matter* **5**, 1760-1791, doi:10.1016/j.matt.2022.04.034 (2022).

30 Xia, Q. *et al.* Solar-enhanced lithium extraction with self-sustaining water recycling from salt-lake brines. *Proceedings of the National Academy of Sciences* **121**, e2400159121, doi:10.1073/pnas.2400159121 (2024).

31 Yong, M. *et al.* Sustainable lithium extraction and magnesium hydroxide co-production from salt-lake brines. *Nature Sustainability* **7**, 1662-1671, doi:10.1038/s41893-024-01435-2 (2024).

32 Zhong, H. *et al.* Efficient and Selective Lithium Extraction from Brine Water Via a Photothermal Sandwich Sieve Structure. *Advanced Functional Materials* **35**, 2418358, doi:10.1002/adfm.202418358 (2025).

33 Mousavinezhad, S., Nili, S., Fahimi, A. & Vahidi, E. Environmental impact assessment of direct lithium extraction from brine resources: Global warming potential, land use, water consumption, and charting sustainable scenarios. *Resources, Conservation and Recycling* **205**, 107583, doi:10.1016/j.resconrec.2024.107583 (2024).

34 Rentier, E. S., Hoorn, C. & Seijmonsbergen, A. C. Lithium brine mining affects geodiversity and Sustainable Development Goals. *Renewable and Sustainable Energy Reviews* **202**, 114642, doi:https://doi.org/10.1016/j.rser.2024.114642 (2024).

35 Williams, G. D. Z. & Vengosh, A. Quality of Wastewater from Lithium-Brine Mining. *Environmental Science & Technology Letters* **12**, 151-157, doi:10.1021/acs.estlett.4c01124 (2025).

36 Wang, S., Stahlbuhk, A. & Steiger, M. Hydration and deliquescence behavior of calcium chloride hydrates. *Fluid Phase Equilibria* **585**, 114171, doi:https://doi.org/10.1016/j.fluid.2024.114171

(2024).
37 Watt, I. C. & D'Arcy, R. L. Hydration of biopolymers. *Journal of Polymer Science: Polymer Symposia* **55**, 155-166, doi:10.1002/polc.5070550117 (1976).
38 Wise, M. E., Martin, S. T., Russell, L. M. & Buseck, P. R. Water Uptake by NaCl Particles Prior to Deliquescence and the Phase Rule. *Aerosol Science and Technology* **42**, 281-294, doi:10.1080/02786820802047115 (2008).
39 Castarède, D. & Thomson, E. S. A thermodynamic description for the hygroscopic growth of atmospheric aerosol particles. *Atmos. Chem. Phys.* **18**, 14939-14948, doi:10.5194/acp-18-14939-2018 (2018).
40 Laskina, O. *et al.* Size Matters in the Water Uptake and Hygroscopic Growth of Atmospherically Relevant Multicomponent Aerosol Particles. *The Journal of Physical Chemistry A* **119**, 4489-4497, doi:10.1021/jp510268p (2015).
41 Gupta, D., Eom, H. J., Cho, H. R. & Ro, C. U. Hygroscopic behavior of NaCl–MgCl₂ mixture particles as nascent sea-spray aerosol surrogates and observation of efflorescence during humidification. *Atmos. Chem. Phys.* **15**, 11273-11290, doi:10.5194/acp-15-11273-2015 (2015).
42 Yao, W., Yu, X., Lee, J. W., Yuan, X. & Schmidt, S. J. Measuring the Deliquescence Point of Crystalline Sucrose as a Function of Temperature Using a New Automatic Isotherm Generator. *International Journal of Food Properties* **14**, 882-893, doi:10.1080/10942910903474393 (2011).
43 Peng, C., Chen, L. & Tang, M. A database for deliquescence and efflorescence relative humidities of compounds with atmospheric relevance. *Fundamental Research* **2**, 578-587, doi:https://doi.org/10.1016/j.fmre.2021.11.021 (2022).
44 Flexer, V., Baspineiro, C. F. & Galli, C. I. Lithium recovery from brines: A vital raw material for green energies with a potential environmental impact in its mining and processing. *Science of The Total Environment* **639**, 1188-1204, doi:10.1016/j.scitotenv.2018.05.223 (2018).
45 Al-Handawi, M. B. *et al.* Harvesting of aerial humidity with natural hygroscopic salt excretions. *Proceedings of the National Academy of Sciences* **120**, e2313134120, doi:10.1073/pnas.2313134120 (2023).
46 Steiger, M., Linnow, K., Ehrhardt, D. & Rohde, M. Decomposition reactions of magnesium sulfate hydrates and phase equilibria in the MgSO4–H2O and Na+–Mg2+–Cl−–SO42−–H2O systems with implications for Mars. *Geochimica et Cosmochimica Acta* **75**, 3600-3626, doi:https://doi.org/10.1016/j.gca.2011.03.038 (2011).
47 Feng, Y. *et al.* A rationally designed scalable thin film nanocomposite cation exchange membrane for precise lithium extraction. *Nature Communications* **16**, 8618, doi:10.1038/s41467-025-63660-3 (2025).
48 Zhang, G. *et al.* Spontaneous lithium extraction and enrichment from brine with net energy output driven by counter-ion gradients. *Nature Water* **2**, 1091-1101, doi:10.1038/s44221-024-00326-2 (2024).
49 Wang, L. *et al.* Redox Flow Battery for Continuous and Energy-Effective Lithium Recovery from Aqueous Solution. *ACS Energy Letters* **7**, 3539-3544, doi:10.1021/acsenergylett.2c01746 (2022).
50 Li, Z. *et al.* Lithium extraction from brine through a decoupled and membrane-free electrochemical cell design. *Science* **385**, 1438-1444, doi:10.1126/science.adg8487 (2024).
51 Watt, I. C. & and D'Arcy, R. L. 26—WATER-VAPOUR ADSORPTION ISOTHERMS OF WOOL. *The Journal of The Textile Institute* **70**, 298-307, doi:10.1080/00405007908658854 (1979).
52 Nandan, D., Venkataramani, B. & Gupta, A. R. Ionic hydration and water sorption isotherms of ion exchange resins. *Langmuir* **9**, 1786-1793, doi:10.1021/la00031a029 (1993).

Acknowledgments

The authors appreciate the support from the National Science Foundation (PFI-2329835) and Princeton Catalysis Initiative (PCI). We acknowledge the use of Princeton's Imaging and Analysis Center, which is partially supported through the Princeton Center for Complex Materials (PCCM), a National Science Foundation (NSF)-MRSEC program (DMR-2011750).

Author Contributions Statement

H.C., Z.J.R. and S.Z. conceived the initial idea. H.C., M.Y., R.S.K., and Z.J.R. contributed to the experimental design. Z.J.R. supervised the study. H.C. and M.Y. conducted materials preparation and system operation. H.C. carried out model development with the help of R.S.K.. H.C. conducted material characterization with the help of M.Y. and A.S.K.. H.C. and H.W. conducted pilot tests for scale-up demonstration. H.C. and Z.J.R. wrote the paper, and all authors commented on the final manuscript.

Competing Interests Statement

H.C., Z.J.R, and S.Z. are authors on a patent application on the same topic (APPLICATION#: 63/854,073). S.Z. and Z.J.R. are co-founders of Princeton Critical Minerals, Inc., and A.K. is a shareholder. The remaining authors declare no competing interests.

Figure Legends/Captions

Fig. 1 Hygroscopicity-driven selective Li extraction and recovery from solid sources such as mining slag deposits, spent battery electrodes, and pharmaceutical wastes. Leveraging the uniquely strong hygroscopicity of LiCl hydrate (LHT), successive low-humidity air exposures induce its moisture uptake and selective dissolution of the Li-bearing phase for recovery, while co-minerals (halite, sylvite, bischofite, gypsum) remain undissolved. This spontaneous process allows rapid solid-liquid separation, yielding ~97% Li recovery in the enriched solution with 1,500× purity enhancement. This greatly accelerates the traditional leaching process from months to a few hours. Distinguished from other extraction processes, this entropy-increasing process uses minimal energy and no chemical or external water. Free icons are sourced from Flaticon (www.flaticon.com) in public domain, all confirmed for commercial publication.

Fig. 2 Mechanism and thermodynamics of selective Li extraction via hygroscopicity under controlled relative humidity (RH). a, Stepwise moisture uptake (g H_2O g^{-1} mineral) for LiCl hydrate (LHT), bischofite, halite, sylvite and gypsum as RH increases from 12% to 96% at 25°C (1 h per step). Darker bars show incremental uptake at each RH; light shading indicates the cumulative uptake at the previous step. Error bars = ± 1 SD (n = 3). b, Limiting RH for each mineral and definition of the effective separation zone (RH 12-30%), subdivided into subzones of RH 12-18%, 18-24% and 24-30%. c,d, Photographs of solids before and after exposure to RH 12-18% (c) and 24-30% (d), with a ~5.2-fold larger solution volume observed at the higher RH range. LHT (left) transforms into a Li-rich solution (right) while co-minerals (halite, sylvite, bischofite, gypsum; bottom row) remain solid. e, Equilibrium moisture uptake isotherm for LHT (θ vs. water activity $a_w = \mathrm{RH}/100$; 6 h per step) with three-term D'Arcy-Watt model fitting (inset). Error bars = ± 1 SD (n = 3). f, Free-energy change $\Delta G = \theta RT \ln a_w$, plotted against θ. Error bars of ΔG = ± 1 SD (n = 3).

Transition from RH 12-18% to 24-30% yields a ~16× increase in Δ*G*, indicating enhanced thermodynamic driving force for moisture adsorption. g, Schematic of the three adsorption contributions in the D'Arcy-Watt model: Term 3 (multi-molecular adsorption) dominates at low RH; Terms 1 (Langmuir) and 2 (linear adsorption) become significant above RH 18%.

Fig. 3 In-situ SEM-EDS analysis and moisture uptake kinetics of hygroscopic Li extraction. a,b, SEM images (left) and corresponding EDS elemental mappings (right) of LiCl hydrate (LHT) in contact with halite, sylvite, bischofite and gypsum (top to bottom) before (a) and after (b) 30 s moisture uptake at RH 24-30%. Moisture originates within LHT, producing a Li-rich solution (appearing as EDS "voids") that advances into adjacent mineral grains, promoting their gradual dissolution. EDS mapping of Cl in Supplementary Fig. 10 also proves similar observation. c, Schematic of the humidity-controlled vacuum-filtration setup. d, Normalized moisture uptake rate (R_{uptake}) plotted against moisture flow rate (R_{flow}). Data follows a Power-Law trend (dash line, R^2 = 0.985), with moisture uptake accelerating markedly when the flow rate exceeds 10 m min^{-1}.

Fig. 4 Li extraction and recovery performance in binary mineral mixtures. Panels a-d show results for Li/Na (LHT/halite), Li/K (LHT/sylvite), Li/Mg (LHT/bischofite) and Li/Ca (LHT/gypsum) systems, respectively, with initial Li/M (M represents Na, K, Mg, or Ca) feeding weight ratios from 1:100 to 50:1, representing low- to high-grade resources. LHT represents LiCl hydrate. For each panel, the top graph displays Li selectivity (columns, left axis) and solution purity (Li/M ratio; spherical dots, right axis) for each extraction batch (error bars = ± 1 SD from at least three independent tests). The bottom plot shows accumulative Li recovery (%) vs. elapsed time, with horizontal marker color bars indicating Li concentration in that batch's solution (g L^{-1}; color scale at bottom).

Fig. 5 Application demonstration in real-world scenarios. a, c-f, Performances of Li extraction and recovery from Li brine mining slags, respectively under the control condition (i.e. relative humidity 24-30% and moisture flow rate 20 m min^{-1}) (a), and the spring condition (c), summer condition (d), fall condition (e), and winter condition (f) of a typical site of evaporation ponds operated in Atacama. The seasonal natural climate data of the mining site is displayed in b. For each condition, two sections are provided left and right to evaluate Li extraction and recovery performances. Solution Li/M (M represents Na, K, Mg, or Ca) ratio (Li purity) and Li selectivity in the solution collected from each batch are displayed in the left section (error bars = ± 1 SD) (n = 3). The digit labeled next to each data point represents the batch number. The shapes of data points index different Li/M pairs involved. The size of the data points represents the concentration of Li in the solution collected from each batch, as clearly stated in figure keys. Progressive Li recovery and processing time are displayed in the right section.

Fig. 6 Modular scale-up demonstration for hygroscopic lithium extraction from industrial slags. a, Photograph (left) and schematic (right) of the inward double-frame module. Li-bearing slags are packed within the hollow interlayer between inner and outer frames and retained by non-woven fiber barriers (see Supplementary Fig. 19). Vacuum applied to the inner chamber draws moisture-laden air through the slag bed, inducing hygroscopic deliquescence and generating Li-rich concentrates that drain across the inner non-woven fiber barrier and then drip into the bottom collector by gravity. b, Top-view image showing spontaneous dripping of Li concentrate into the collector. c, Slag processing rate (red, normalized by module height) and Li concentrate yield (blue) as functions of air flow (50-100 L min^{-1}) under favorable conditions (relative humidity 24-30%) (error bars = ± 1 SD) (n = 3). d, Area-normalized Li extraction rates vs. Li concentration in collected solutions, benchmarked against representative Li extraction technologies from the literatures[27,47-50].

Editorial Summary:

This work shows humidity-controlled hygroscopic deliquescence as an entropy increasing route for spontaneous lithium extraction from complex mining slags, enabling rapid, selective recovery in ambient conditions with scalable, low-energy potential.

Peer review information: *Nature Communications* thanks Xiangrui Kong, and the other, anonymous, reviewer(s) for their contribution to the peer review of this work. A peer review file is available.

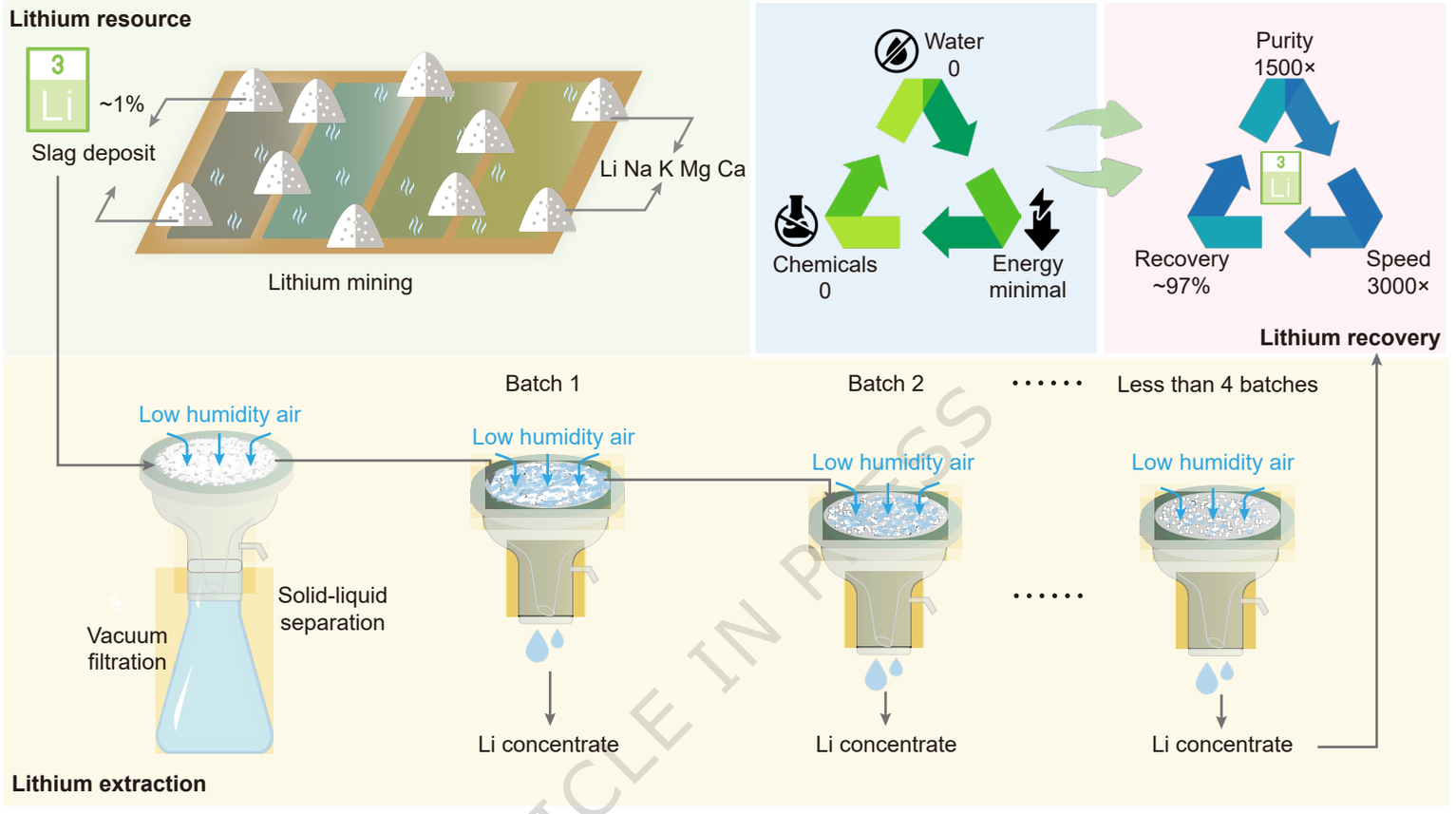

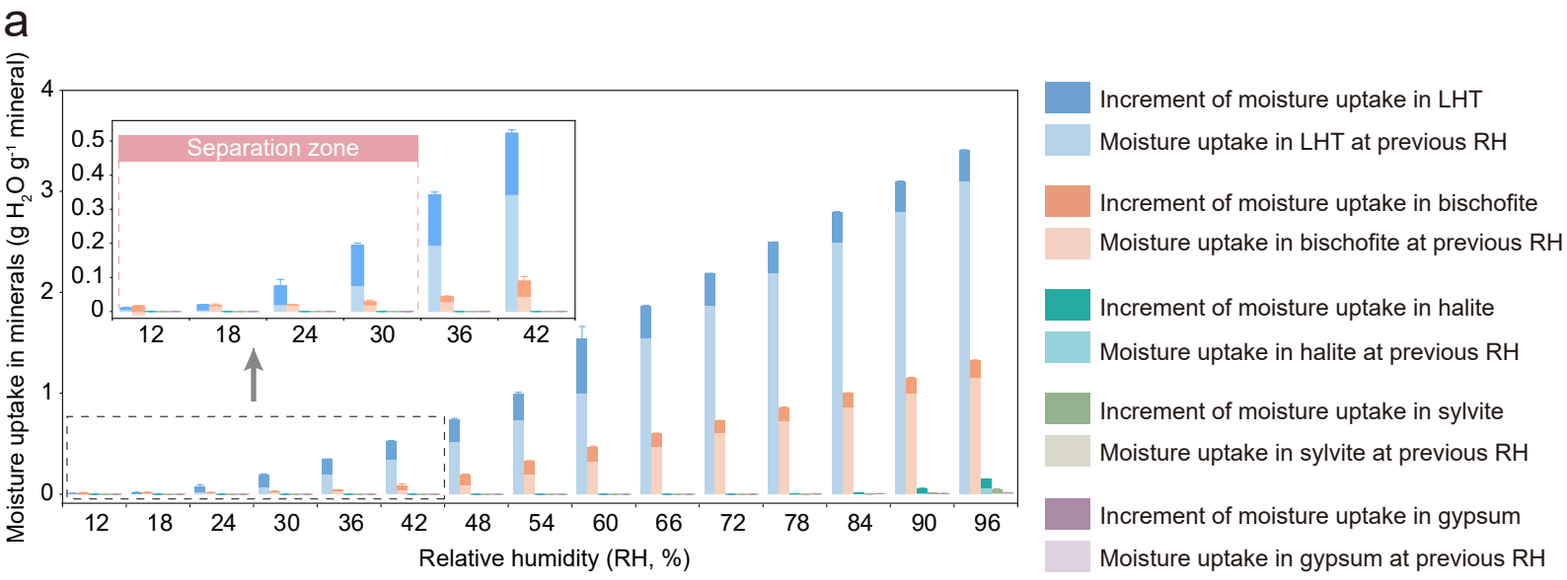

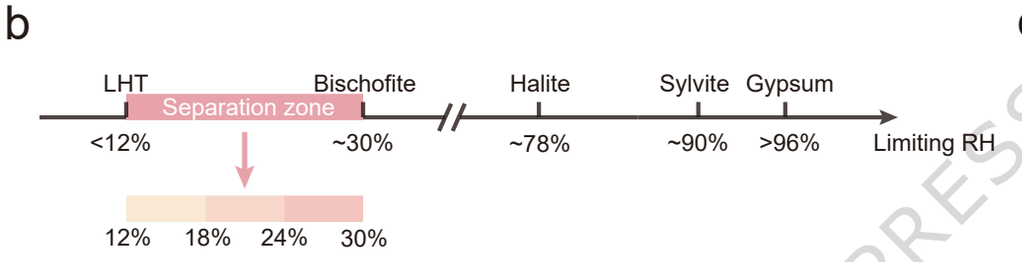

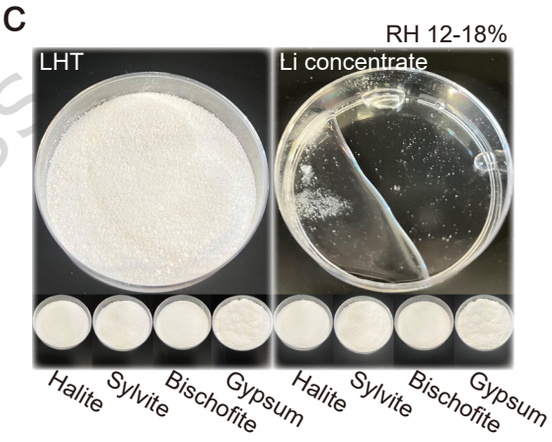

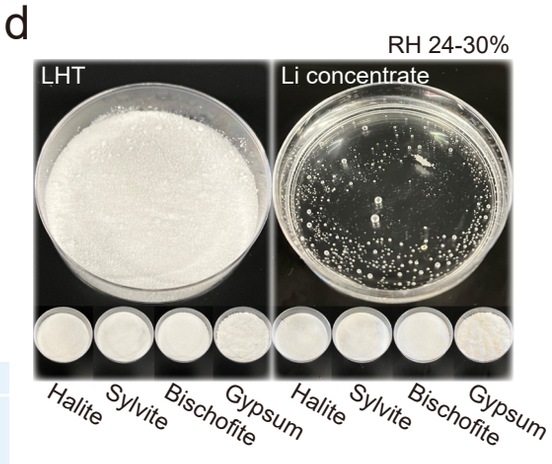

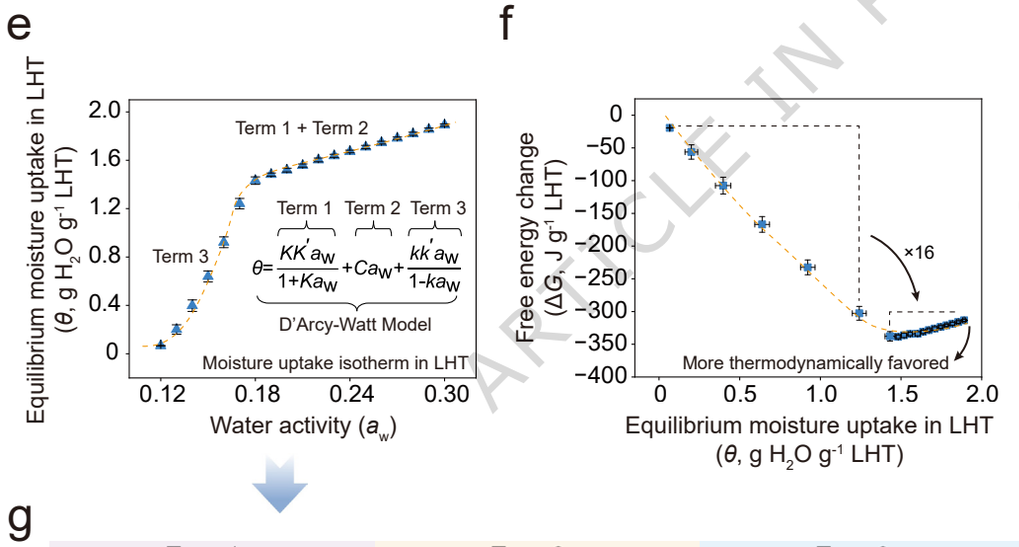

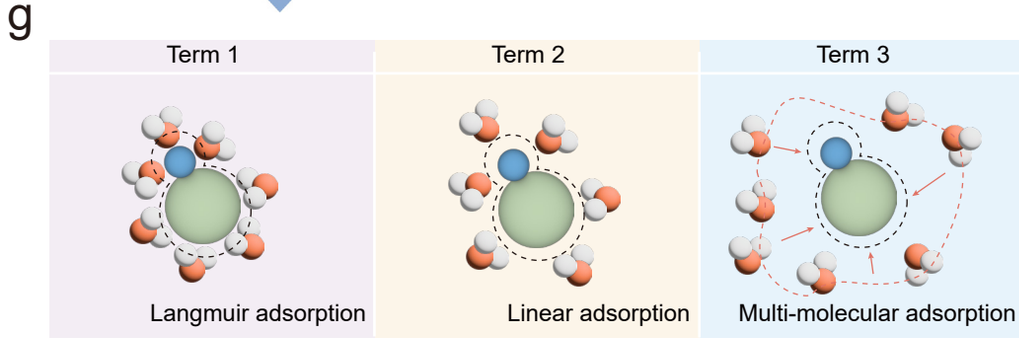

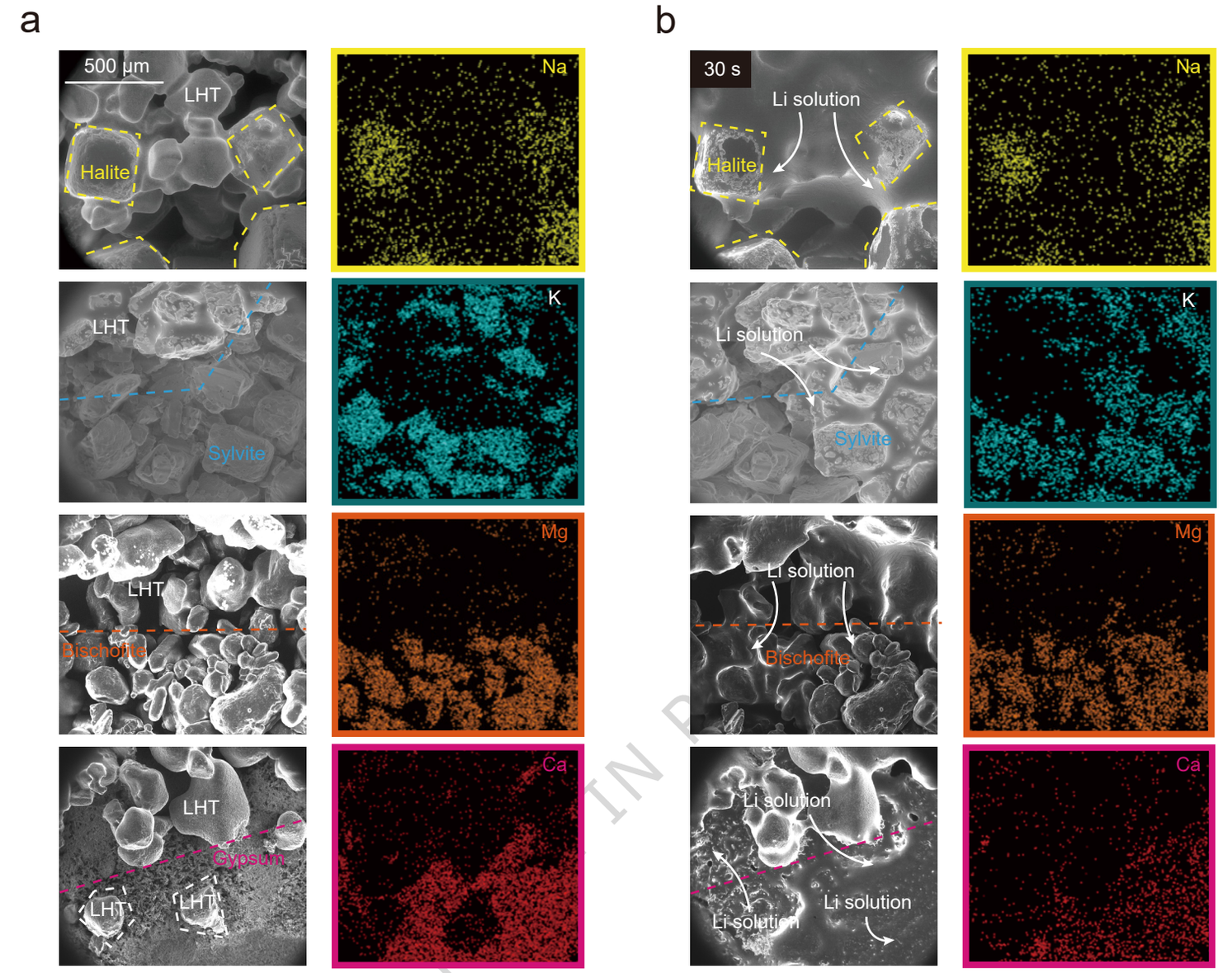
a
500 μm
LHT
Halite
Na
LHT
Sylvite
K
LHT
Bischofite
Mg
LHT
Gypsum
LHT
LHT
Ca
b
30 s
Li solution
Halite
Na
Li solution
Sylvite
K
Li solution
Bischofite
Mg
Li solution
Li solution
Li solution
Ca

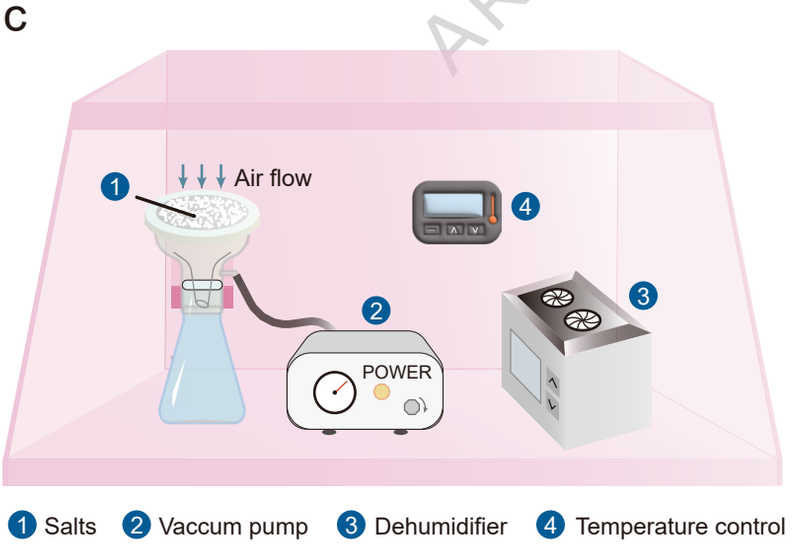
c
Air flow
POWER
1 Salts
2 Vaccum pump
3 Dehumidifier
4 Temperature control

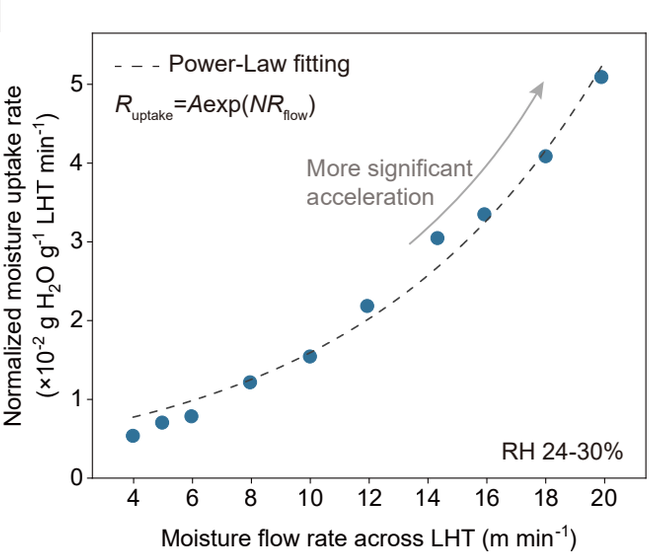
d
Power-Law fitting
R_{uptake}=Aexp(NR_{flow})
More significant acceleration
RH 24-30%
Normalized moisture uptake rate (×10^{-2} g H_2O g^{-1} LHT min^{-1})
Moisture flow rate across LHT (m min^{-1})
0
1
2
3
4
5
4
6
8
10
12
14
16
18
20